Manuscript refereed by Mr James Shipley (Quintus Technologies AB, Sweden)

Influence Of The Powder Particle Size Distribution On The Microstructure Of Laser Powder Bed Alloyed Cold Work Tool Steel

Marie Luise Köhler[1], Simone Herzog[1], Anke Kaletsch[1], Christoph Broeckmann[1]
[1]Institute for Materials Applications in Mechanical Engineering, RWTH Aachen University, Germany

Abstract:
Carbide-rich tool steels are known to be difficult to process by Laser Powder Bed Fusion (LPBF). In order to enhance processability and mechanical properties, alloy development is required. Simultaneously, powder mixtures as feedstock for the LPBF process become increasingly attractive for researchers, as this is a cost-efficient way of alloy development. A high chromium alloyed cold work tool steel, based on conventionally available AISI H13 powder and modified by additions of Cr_3C_2, Cr and FeCrC powder was processed by LPBF. Different powder particle size distributions were used to characterize their influence on the microstructure of the cold work tool steel. The microstructure is analysed in detail by light optical microscopy, backscattered electron imaging and electron backscatter diffraction. The resulting chemical homogeneity and mechanical properties of the steel are further analysed by optical emission spectroscopy, energy dispersive X-ray spectroscopy and hardness testing.

Keywords: Powder blend, Particle Size distribution, Laser Powder Bed Fusion, Microstructure

1. Introduction:

The effect of the Laser powder bed fusion (LPBF) process on steels with higher carbon contents, e.g. cold-work and high-speed steels, has hardly been investigated. High carbon steels show a tendency for cold crack formation during LPBF processing. These cold cracks are attributed to large internal stresses from the high temperature gradients and complex thermal profiles within the built-up structure [1]. The fast solidification of the alloy leads to the formation of metastable phases. A local enrichment of the austenite with alloying elements leads to the lowering of the martensite transformation temperature. Retained austenite decreases the alloy's crack susceptibility due to its enhanced ductility. [2,3]

Laser Powder Bed alloying (LPBA) has recently attained the attention of many researchers as it provides a cheap but effective method of receiving alloy compositions of interest without expensive atomization of small powder batches for experimental build-jobs. Various researchers have analysed the influence of mechanical mixing and the resulting microstructure of their alloys. The spectrum includes various materials (steel, high entropy alloys, non-ferrous alloys) as well as mixtures of pre-alloyed and/ or elemental powders. [4–7]

Only lately has the research also focussed on influencing factors for successful LPBA. Previously, results have been shown and problems such as undissolved particles and chemical inhomogeneity were described.[6] The powder morphology and particle size distribution (PSD) are known to play a significant role in the processing of powder blends by LPBA [8].

This research aims at providing insights to LPBA of cold work tool steels. The PSD of the main component of a powder blend is varied. The additions to this base component are kept identical to clearly evaluate the influence of the main components' PSD on the processability of LPBA cold work tool steel.

2. Materials and methods

A target alloy composition similar to a standard corrosion resistant martensitic steel AISI 440C (DIN X105CrMo17, EN 1.4125) was chosen and realized by blending four commercially available powders. The alloy is based on AISI H13 (DIN X40CrMoV5-1, EN 1.2344) and modified by additions of FeCrC, Cr_3C_2 and elemental Cr in the mass ratio 88:7:5:5. The AISI H13, Cr and FeCrC powders have been gas atomized and thus are spherical whereas the Cr_3C_2 powder is mechanically crushed with an irregular shape. The alloying content of the powders and the calculated composition from the mixing ratio are listed in Table 1. The nominal composition of the AISI 440C is provided for comparison.

Table 1: Nominal chemical composition of utilized base steels and calculated composition of the powder mixtures [wt.-%], complemented by the theoretical density ρ of each component

Name	C	Si	Mn	Cr	Mo	V	Fe	ρ [g/cm²]
AISI H13	0.4	1.0	0.5	5.3	1.3	1.0	90.5.	7.7
FeCrC	3.9	0.5	-	31.0	-	-	64.6	7.5
Cr_3C_2	13.3	-	-	86.7	-	-	-	6.7
Cr	-	-	-	100	-	-	-	7.2
88:7:5:5	1.22	0.84	0.42	15.4	1.09	0.84	80.2	
AISI 440 C	1.05	-	-	17.0	0.75	-	81.7	

Two PSDs of the AISI H13 powder are used to identify the influence of the chosen PSD on the resulting homogeneity of the microstructure. The powders were blended in a tumble mixer for 30 min immediately prior to being processed by LPBA. The PSD of the powders was determined by a Camsizer X2 (Microtrac Retsch GmbH) and is provided in Table 2. The two blended alloys 88:7:5:5 with finer AISI H13 particles and 88:7:5:5 with larger AISI H13 particles are hereafter named A1 and A2 respectively. The flowability and apparent density of A1 and A2 were characterized with a Hall Flowmeter according to ISO 4490:2018. Secondary electron (SE) images of A1 and A2 are provided in

Figure 1.

Table 2: PSD of the utilized powders.

	D10 [µm]	D50 [µm]	D90 [µm]
AISI H13 – 1	8.6	17.2	28.5
AISI H13 – 2	27.4	41.1	58.8
FeCrC	10.0	22.3	39.2
Cr	21.0	37.2	54.0
Cr_3C_2	3.4	7.1	10.4
A1	7.2	17.4	31.8
A2	22.2	38.5	52.0

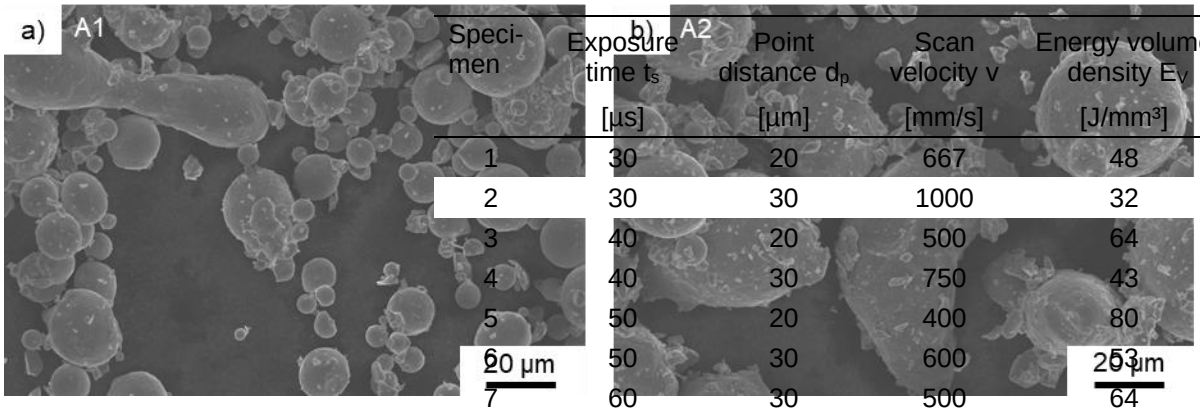

Speci-men	Exposure time t_s [µs]	Point distance d_p [µm]	Scan velocity v [mm/s]	Energy volume density E_V [J/mm³]
1	30	20	667	48
2	30	30	1000	32
3	40	20	500	64
4	40	30	750	43
5	50	20	400	80
6	50	30	600	53
7	60	30	500	64
8	60	40	667	48
9	70	30	429	75
10	70	40	571	56
11	80	40	500	64
12	80	50	625	51

Speci-men	Exposure time t_s [µs]	Point distance d_p [µm]	Scan velocity v [mm/s]	Energy volume density E_V [J/mm³]
1	30	20	667	48
2	30	30	1000	32
3	40	20	500	64
4	40	30	750	43
5	50	20	400	80
6	50	30	600	53
7	60	30	500	64

Figure 1: SE images of powder blends a) A1 and b) A2.

2.1.Sample production

10 mm x 10 mm x 10 mm cubic specimens for metallographic characterization were produced with a Realizer SLM 100 machine which is equipped with a pulsating Ytterbium fibre laser. The scan velocity v is defined by the point distance d_p and exposure time t_s. The layer thickness was set to 50 µm and a laser power of 160 W was applied. A detailed description of the varied processing parameters for the samples is provided in **Error! Reference source not found.**. A hatch distance of 100 µm was used for all samples. The hatch direction was rotated by 90° after each layer. A building plate preheating temperature of 500 °C was applied and argon was used as process gas. The recoating velocity of the radial recoater is pre-set to 19 °/s.

8	60	40	667	48
9	70	30	429	75
10	70	40	571	56
11	80	40	500	64
12	80	50	625	51

Table 3: Varied process parameters for sample production.

2.2 Microstructural analysis

The cubes were cut vertically parallel to the building direction, the surface was ground and polished. Light optical microscope (LOM) images of unetched samples were used to determine the relative density of the samples by means of image analysis. Greyscale images of the cross section with a magnitude of x100 were used for this purpose. The fraction between black and white areas was determined using Fiji-ImageJ software [9], as pores appearing in black reduce the relative density. Five pictures per sample from different locations in the sample were used for statistical reasons to quantify the relative density.

Electron backscatter diffraction (EBSD) was used to locally analyse phase fractions and reveal retained austenite. The step size was set to 0.1 µm. Pre-defined phases were fcc austenite and bcc ferrite. Backscatter electron images (BSE) supported by energy dispersive X-ray spectroscopy (EDS) measurements were conducted to show chemical inhomogeneity within the microstructure. The scans were performed on a Helios NanoLab DualBeam Scanning Electron Microscope.

Hardness (Vickers HV 10) was tested according to DIN EN ISO 6507. The hardness indentations were placed over the height of the vertically cut cross sections of the specimens.

3. Results and Discussion

The powder beds during the build process of A1 and A2 are shown in Figure 2. The recoating direction is indicated by the red arrows. The powder bed of A1 shows a colour difference between the top left corner and the bottom right corner, directly correlating with the recoating direction. A larger PSD of the alloy as used in A2 only shows slight traces of the recoating direction in the powder bed with a more homogeneous powder bed. Demixing is assumed to be dependent on recoating velocity as the absolute velocity varies with the distance from the turning point (top left corner, beyond the range of the image).

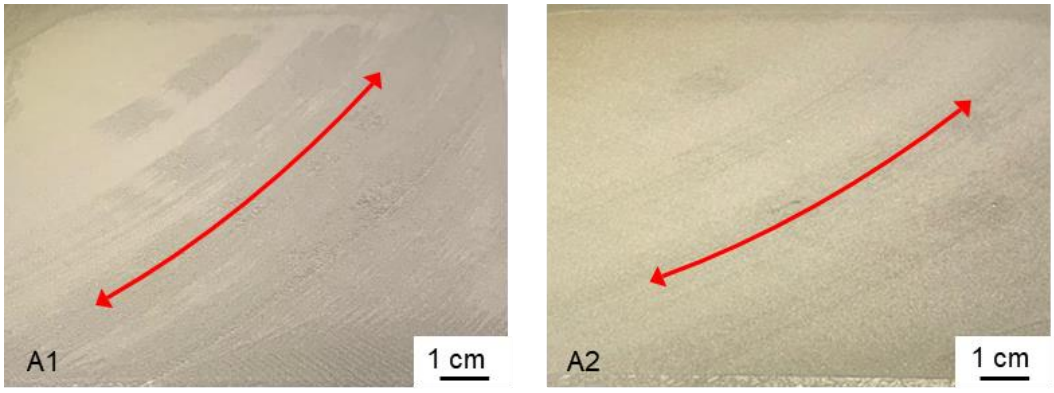

Figure 2: Powder bed during the build-up of cubic specimen of the two alloys. Red markings represent the recoating direction.

The flowability and apparent density measurements were performed to characterize the difference in the powder behaviour. According to ISO 4490:2018 both powder blends are not flowable delivering no indication of better processability of A2 compared to A1. The apparent density of A1 is 3.78 g/cm³ and therefore slightly higher than A2 which has an apparent density of 3.67 g/cm³.

All cubes show no macroscopic cracks after processing. The build plate of A2 is exemplarily shown in Figure 3. OES measurements of the marked specimens were performed to analyze the influence of the recoating and the powder bed inhomogeneity on the chemical composition of the cubes.

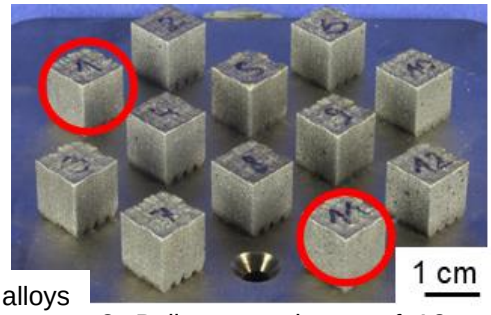

3: Built-up specimens of A2 on ate plate, red markings indicate ens used for macroscopic cal analysis by OES.

The results of the OES measurements are provided in Deviations in the chromium and carbon content of the alloy can directly be attributed to a demixing of fine Cr_3C_2 particles and larger Cr particles. The iron content of the Cr enriched specimen A1-11 is lowered by almost the exact amount of Cr enrichment (1%) suggesting that the FeCrC powder does not participate in the demixing. This assumption allows calculating the amount of Cr and Cr_3C_2 dissolved in the specimens. Both analysed specimens of A2 dissolved 5.2% Cr and 4.5% Cr_3C_2. Specimen A1-1 contains 4.1% Cr and 3.3% Cr_3C_2 whereas specimen A1-11 contains 4.9% Cr and 3.8% Cr_3C_2. These calculations are subject to measurement inaccuracy and to be considered carefully. The results of the calculations on dissolved components suggest a demixing tendency of coarse and fine particles depending on the PSD of the main component. AISI H13-2 has a similar PSD as the elemental Cr, resulting in less demixing of Cr in A2. Larger particles of the main component seem to additionally prevent the demixing of fine Cr_3C_2 particles in the powder bed. The theoretical density of the powders is considered neglectable in terms of the demixing phenomena as all powders lie in the range of 6.7 to 7.7 g/cm³.

Table 4: OES measurements of specimen 1 and 11 of the alloys A1 and A2 complemented by the ideal calculated composition; Strong deviations from the ideal composition are marked in red.

Name	C	Si	Mn	Cr	Mo	V	Fe
A1-1	1.05	0.9	0.4	13.6	1.3	0.8	81.6
A1-11	1.10	0.9	0.4	14.7	1.3	0.7	80.6
A2-1	1.19	0.7	0.3	15.6	1.2	0.9	79.5
A2-11	1.20	0.7	0.3	15.7	1.2	0.9	79.4
88:7:5:5	1.22	0.8	0.4	15.4	1.1	0.8	80.2

. The calculated composition of 88:7:5:5 is provided as reference. Red values highlight deviations within the build plate from the ideal composition. Deviations in the chromium and carbon content of the alloy can directly be attributed to a demixing of fine Cr_3C_2 particles and larger Cr particles. The iron content of the Cr enriched specimen A1-11 is lowered by almost the exact amount of Cr enrichment (1%) suggesting that the FeCrC powder does not participate in the demixing. This assumption allows calculating the amount of Cr and Cr_3C_2 dissolved in the specimens. Both analysed specimens of A2 dissolved 5.2% Cr and 4.5% Cr_3C_2. Specimen A1-1 contains 4.1% Cr and 3.3% Cr_3C_2 whereas specimen A1-11 contains 4.9% Cr and 3.8% Cr_3C_2. These calculations are subject to measurement inaccuracy and to be considered carefully. The results of the calculations on dissolved components suggest a demixing tendency of coarse and fine particles depending on the PSD of the main component. AISI H13-2 has a similar PSD as the elemental Cr, resulting in less demixing of Cr in A2. Larger particles of the main component seem to additionally prevent the demixing of fine Cr_3C_2 particles in the powder bed. The theoretical density of the powders is considered neglectable in terms of the demixing phenomena as all powders lie in the range of 6.7 to 7.7 g/cm³.

Porosity analysis of the A1 specimens revealed the lowest porosity in the specimens with low E_V. The minimal porosity was achieved with 0.15% in specimen 2 (E_V = 32 J/mm³). With a gradual increase in E_V the porosity increases simultaneously, reaching up to 1.49% at 75 J/mm³ (specimen 9). The same observation is valid for A2 where the lowest porosity is also achieved in specimen 2 (E_V = 32 J/mm³) with 0.06%.

The difference in the chemical composition of A1 specimen, related to the powder bed demixing phenomena, leads to a limited possibility of interpreting the results. Based on the positioning of the sample in the powder bed the amount of powder additives differs in the sample set. Further analyses are therefore focused on specimens 1, 2 and 4 which showed the highest density and, due to the placement as direct neighbours, can be compared reasonable with one another. Microstructure analysis by BSE imaging showed undissolved Cr-rich inclusions in A1 and A2 as can be seen in black irregular shapes in .

 P

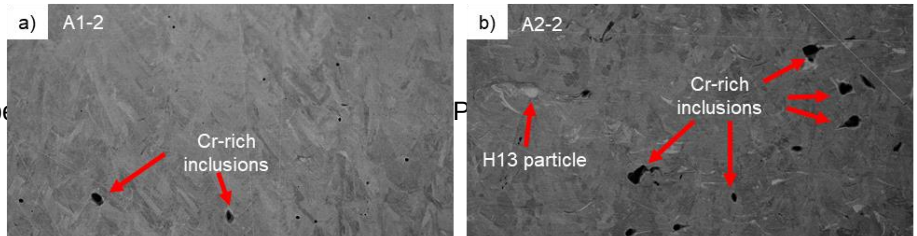

Figure 4: BSE images of a) A1-2 and b) A2-2 (both E_V = 32 J/mm³).

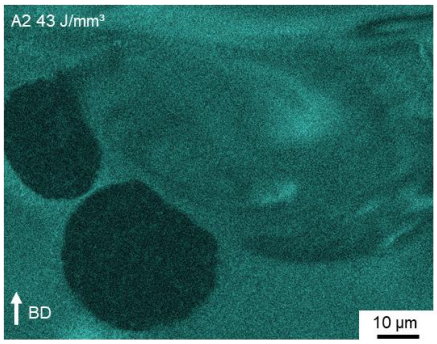

Figure 5: EDS mapping of the Cr content of a meltpool in specimen A2-4 (E_V = 43 J/mm³) with unmolten AISI H13 particles at the meltpool border.

These inclusions are clearly identified by EDS measurements to be Cr and C-rich accompanied by O. Complementary analyses of alloys without elemental Cr do not show these inclusions whereas if the other components are exchanged they are still apparent. Possibly the elemental chromium reacts with C from the melt and O from possibly oxide coated elemental Cr or the process atmosphere during solidification forming these inclusions. Randomly chosen areas within the specimens A1-2 and A2-2 suggest a higher amount of inclusions in A2, possibly being connected with the macroscopically lower Cr content in the powder bed in A1, but could also be due to better homogenization of the alloy in the chosen parameter set.

Bright areas, as to be observed in A2-2, are identified to be partially molten AISI H13 particles by EDS. An EDS mapping of A2-4 (E_V = 43 J/mm³) is shown in Figure 5. The particles appear partially molten in some areas whereas in others they are perfectly spherical having the diameter of original AISI H13 particles. These areas of Cr depletions are observed in all analysed specimens of A2. In all cases, these chromium depletions do not appear with porosity, thus are not connected to lack of fusion defects in the microstructure. Cr depleted areas from unmolten H13 particles are not observed anywhere in A1. The liquidus temperature of AISI H13 (1645°C) is lower than that of elemental chromium (1907 °C) and that of Cr_3C_2 (1895°C). The liquidus temperature of FeCrC is approximately 1325°C and therefore lower than AISI H13. The reason for unmolten AISI H13 in A2 is only partially attributed to the larger size of the particles in A2 compared to A1. Influencing factors could additionally be surface passivation and oxidation. The oxygen content of the powders was not measured and its influence cannot be resolved at this point.

Increasing the energy input in the samples of A2 improves the chemical homogeneity, as depicted in *Figure 6*. Less residual chromium carbides are apparent in specimen 4 (E_V = 48 J/mm³) compared to specimen 1 (E_V = 43 J/mm³) as well as fewer (partially) unmolten AISI H13 particles. Considering the increase in porosity (from 0.06% in A2-2 (E_V = 32 J/mm³) to 0.2% in A2-4 (E_V = 43 J/mm³) vs. 0.3% in A2-1 (E_V = 48 J/mm³)) and the increase in chemical homogeneity a trade-off has to be done when picking the ideal processing parameters. An approach reasonable for homogeneity of the microstructure at low porosity could be to further reduce the size of the chromium carbide particles. In this case the homogeneity of the powder bed needs to be closely monitored in order to get reproducible specimens by LPBA.

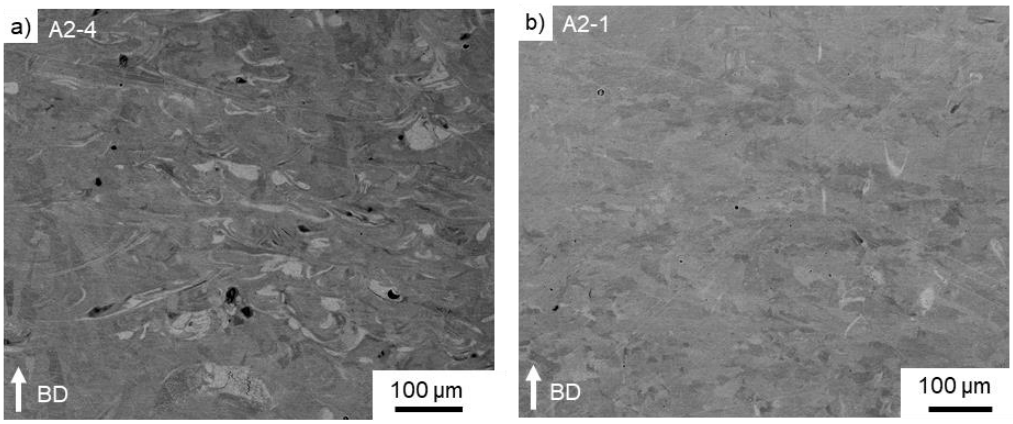

Figure 6: Decreasing chemical inhomogeneity with increasing energy input, shown by BSE images of a) A2-4 (E_V = 43 J/mm³) and b) A2-1 (E_V = 48 J/mm³).

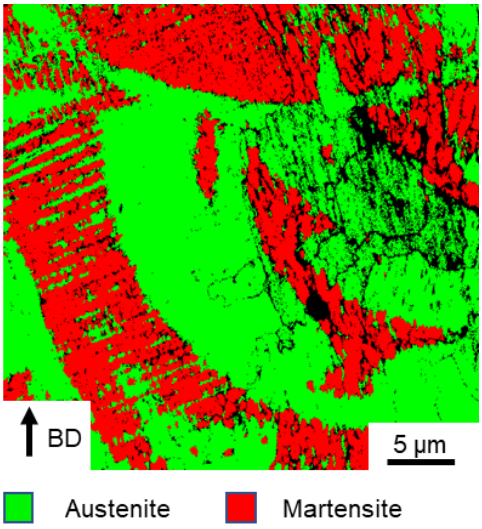

Figure 7: Exemplary EBSD measurement of A1 in the as-built state

The phase fraction of martensite and retained austenite is evaluated by EBSD measurements. Figure 7 shows an EBSD scan of A1. The measurement was performed on a different parameter set specimen than used in this study. Nonetheless, it becomes apparent that high retained austenite contents are stabilized due to the high alloying content. Carbide forming elements are dissolved in the austenite suppressing the martensite finish temperature below room temperature. High retained austenite contents are known to enhance processability in LPBF due to a higher ductility compared to martensite. This observation is valid for the parameter sets used in this study as well as all specimens were crack-free despite the high carbon content of 1.2%

Results of hardness measurements are summarized in Table 5. The hardness is comparably low for cold work tool steels and directly attributed to the high retained austenite content. A hardening process and annealing at a temperature where secondary carbides precipitate from the matrix can be used to deplete the austenite stabilizing elements and to get a transformation from austenite to martensite when quenching the material. The hardness of all samples lies in the same range. Slight variances are attributed to chemical differences in A1 and microstructural inhomogeneity in A2 and cannot be directly correlated to the processing parameters.

Table 5: Hardness measurements of low porosity specimens 1, 2, & 4 of A1 and A2.

E_V/ Specimen	*A1*	*A2*
E_V = 32 J/mm³/ Specimen 2	*419 ± 12 HV10*	*409 ± 8 HV10*
E_V = 43 J/mm³/ Specimen 4	*407 ± 5 HV10*	*407 ± 11 HV10*
E_V = 48 J/mm³/ Specimen 1	*395 ± 10 HV10*	*414 ± 18 HV10*

4. Conclusion and outlook

In order to realize a corrosion resistant tool steel similar to AISI 440C by LPBA, in this study, two blends of AISI H13 with FeCrC, Cr_3C_2, Cr additions were analysed. The PSD of the main component AISI H13 was varied to analyse its influence on the processability and the resulting microstructure. Following conclusions are drawn from the microstructure analysis:

- Crack-free specimens were built up by LPBA with a carbon content of up to 1.2%. The good processability is attributed to high levels of retained austenite.
- Depending on the PSD of the main component of the powder blend different demixing tendencies are observed during recoating in the powder bed. Larger and smaller particles compared to the main component tend to drift towards the outer rim of the radial movement of the recoater.

- FeCrC or agglomerated Cr_3C_2 (or both) lead to residual unmolten carbides being present in the microstructure.
- Areas of Cr-depletion attributed to not fully molten AISI H13 are present in the alloy based on a coarse PSD of the main constituent.
- Increasing the energy input leads to higher microstructural homogeneity as well as an increase in porosity.
- The hardness in the as-built state does not reach standards for cold work tool steels which is attributed to high levels of retained austenite.

Additional research needs to be carried out to identify a parameter set for stable chemical and microstructural homogeneity in each position on the build plate. To bring these alloys into industrial application a martensitic microstructure with high abrasion resistance (and corrosion resistance) is required. Further studies include a systematic analysis of the heat treatment conditions and the resulting mechanical properties. The heat treatment can possibly lead to a more homogenous microstructure when diffusion is enabled to eliminate chemical gradients.

Acknowledgements

This work was funded by IGF project 20933 N of the “Forschungsgesellschaft Stahlverformung e.V.” via the AiF as part of the IGF program by the Bundesministerium für Wirtschaft und Energie.

References

[1] K. Kempen, Expanding the materials palette for Selective Laser Melting of metals, 2015.
[2] H. Fayazfar, M. Salarian, A. Rogalsky, D. Sarker, P. Russo, V. Paserin, E. Toyserkani, A critical review of powder-based additive manufacturing of ferrous alloys: Process parameters, microstructure and mechanical properties, Materials & Design 144 (2018) 98–128.
[3] G. Tang, F. Xu, G. Fan, X. Ma, L. Wang, Mechanisms of microstructure formations in M50 steel melted layer by high current pulsed electron beam, Nuclear Instruments and Methods in Physics Research Section B: Beam Interactions with Materials and Atoms 288 (2012) 1–5.
[4] A. Taruttis, C. Hardes, A. Röttger, V. Uhlenwinkel, A.B. Chehreh, W. Theisen, F. Walther et al., Laser additive manufacturing of hot work tool steel by means of a starting powder containing partly spherical pure elements and ferroalloys, Procedia CIRP 94 (2020) 46–51.
[5] L. Shoji Aota, P. Bajaj, H.R. Zschommler Sandim, E. Aimé Jägle, Laser Powder-Bed Fusion as an Alloy Development Tool: Parameter Selection for In-Situ Alloying Using Elemental Powders, Materials (Basel, Switzerland) 13 (2020).
[6] M.H. Mosallanejad, B. Niroumand, A. Aversa, A. Saboori, In-Situ Alloying in Laser-Based Additive Manufacturing Processes: A Critical Review, Journal of Alloys and Compounds 117 (2021) 159567.
[7] A. Katz-Demyanetz, A. Koptyug, V.V. Popov, In-situ Alloying as a Novel Methodology in Additive Manufacturing, in: 2020 IEEE 10th International Conference Nanomaterials: Applications & Properties (NAP), IEEE, 2020 - 2020, 02SAMA05-1-02SAMA05-4.
[8] M.S. Knieps, W.J. Reynolds, J. Dejaune, A.T. Clare, A. Evirgen, In-situ alloying in powder bed fusion: The role of powder morphology, Materials Science and Engineering: A 807 (2021) 140849.
[9] J. Schindelin, I. Arganda-Carreras, E. Frise, V. Kaynig, M. Longair, T. Pietzsch, S. Preibisch et al., Fiji: an open-source platform for biological-image analysis, Nature methods 9 (2012) 676–682.